Joule-Thomson cooling of CO_2 injected into aquifer under heat exchange with adjacent formations by Newton's law- 1D exact solution.

Christina Chesnokov[1], Rouhi Farajzadeh[2,3], Kofi Ohemeng Kyei Prempeh[1], Siavash Kahrobaei[2], Jeroen Snippe[2], Pavel Bedrikovetsky[1]

[1] The University of Adelaide, Australia

[2] Shell Global Solutions International, The Hague, The Netherlands

[3] Delft University of Technology, The Netherlands

Abstract

This paper discusses axi-symmetric flow during CO_2 injection into a non-adiabatic reservoir accounting for Joule-Thomson cooling and steady-state heat exchange between the reservoir and the adjacent layers by Newton's law. An exact solution for this 1D problem is derived and a new method for model validation by comparison with quasi 2D analytical heat-conductivity solution is developed. The temperature profile obtained by the analytical solution shows a temperature decrease to a minimum value, followed by a sharp increase to initial reservoir temperature. The analytical model exhibits stabilisation of the temperature profile and cooled zone. When accounting for heat gain from adjacent layers, the minimum temperature is higher compared to the case with no heat exchange. The analytical model can be used to evaluate the risks of hydrate formation and/or rock integrity during CO_2 storage in depleted reservoirs.

Keywords: CO_2 storage, Joule-Thomson, Heat exchange, Newton's law, Analytical model, Aquifer.

Nomenclature

a_a	Thermal diffusivity of adjacent formations	m^2/s
A^*	Dimensionless J-T number	[-]
B	Dimensional heat exchange	m^{-3}
C	Dimensional heat exchange for steady state case	m^{-2}
D	Dimensional J-T number for steady state case	K m
c_s	Heat capacity of reservoir rock	J/kg/K
c_w	Heat capacity of water	J/kg/K

c_f	Heat capacity of CO_2	J/kg/K
c_{ra}	Heat capacity of adjacent formation rock	J/kg/K
c^{res}	Overall reservoir heat capacity	J/ m^3/K
c^a	Overall adjacent formation heat capacity	J/ m^3/K
H	Formation thickness	m
k	Permeability	m^2
k_{rf}^e	End-point relative permeability of CO_2	[-]
l	Shale thickness	m
M_J	Mass injection rate	kg/s
p	Fluid pressure	Pa
p_J	Injection pressure of CO_2	Pa
p_w	Reservoir pressure	Pa
q_J	CO_2 injection rate	m^3/s
r	Radial distance along flow direction	m
r_D	Dimensionless radial distance along flow direction	[-]
r_w	Well radius	m
r_f	CO_2 front position	m
r_{norm}	Normalized distance	[-]
r_{inj}	Injection radius	m
r_p	Temperature penetration depth radius	m
r_c	Critical radius of validity	[-]
S_{wi}	Connate water saturation	[-]
T	Temperature	K
T_I	Initial reservoir temperature	K
T_J	Injection temperature	K
T_D	Dimensionless reservoir temperature	[-]
T_{min}	Minimum reservoir temperature	K
t	Time	s

t_0	Starting time for heat propagation	s
t_{inj}	Injection time	s
t_D	Dimensionless time	[-]
$t_{D\,max}$	Maximum dimensionless time for validity	[-]
V	Dimensional heat front velocity	m^{-1}
V^*	Dimensionless heat front velocity	[-]
x	Spatial integral variable	m
z	Distance along vertical direction for heat flow between layers	m
z_D	Dimensionless vertical coordinate	[-]

Greek letters

α_{JT}	Joule-Thomson coefficient	K/Pa
γ_{ra}	Heat conductivity of adjacent layers	W/m/K
γ_{rs}	Heat conductivity of shale	W/m/K
γ_w	Heat conductivity of water	W/m/K
γ^s	Overall shale heat conductivity	W/m/K
γ^a	Overall adjacent layer heat conductivity	W/m/K
θ	Dimensionless temperature in vertical heat conduction	[-]
κ	Overall heat transfer coefficient of shale	W/m^2/K
μ_f	Viscosity of CO_2	Pa s
ρ_s	Reservoir Rock density	kg/m^3
ρ_w	Water density	kg/m^3
ρ_f	CO_2 density	kg/m^3
ρ_{ra}	Adjacent layers rock density	kg/m^3
τ	Temporal integral variable	s
ϕ	Reservoir Porosity	[-]
ϕ_s	Shale Porosity	[-]
ϕ_a	Adjacent layers Porosity	[-]
ω	Dimensionless Newton's validity parameter	[-]

1. INTRODUCTION

The growing concerns over negative impacts of greenhouse gases, in particular Carbon dioxide (CO_2), on climate change have increased the interest in developing different methods to reduce their emissions into the atmosphere. A practical and complementary solution is to capture CO_2 from highly concentrated sources, e.g., industrial plants or directly from air and store it in underground geological formations such as depleted oil and gas reservoirs, deep saline aquifers, and coal beds.

Depleted gas fields exhibit several advantages over other geological formations. The extracted gas from these fields can in principle be replaced by CO_2 and as such, huge volumes of CO_2 can be stored in these reservoirs. For example, it has been estimated that in the Dutch sector of the North Sea, theoretically, more than 1.5 Gton of CO_2 can be stored in the depleted gas fields (Van der Velde et al., 2008). Due to large recovery factors (extracted fraction of the initial volumes) and compressibility of gas more space is available in the gas fields compared to oil fields, in which the extracted oil is usually replaced by injection of another (usually incompressible) fluids (Hamza et al., 2021).

The production of oil fields often involves injection of external fluids (for pressure maintenance or improved-recovery purposes) and/or drilling of a much larger number of wells, limiting their storage volumes and increasing the risk of leakage pathways (Van der Velde et al., 2008). Compared to aquifers, because of their long production history, the uncertainty in the geological settings (permeability, heterogeneity, faults, fractures, etc.) of the hydrocarbon fields is relatively low. Moreover, these fields have proven seal and containment integrity and have part of the infrastructure required to handle the gas. The sequestration of CO_2 can also be combined with enhancing gas recovery, which could partially compensate for the cost associated with CO_2 sequestration (Battashi et al., 2022; Hamza et al., 2021).

However, there are challenges with CO_2 storage in depleted gas reservoirs, some of which are related to the thermodynamic properties of CO_2. From point of capture (or production) to inside the reservoir pores, CO_2 experiences different pressure and temperature conditions and may exist in gas, liquid or, under certain conditions, solid forms. Of particular concern for CO_2 storage in low-pressure reservoirs is the so-called Joule-Thomson (J-T) cooling effect, which is caused by expansion of CO_2 from high surface pressures to low reservoir pressures.

This is schematically shown by path $A{\rightarrow}D$ in Fig. 1. Point A represents the pressure and the temperature of the transported CO_2 at the storage site, which is assumed to be at 100 bar and 30ºC (i.e., CO_2 is injected in dense liquid

phase). With the assumptions that heat conduction in the wellbore is negligible and that the viscous and gravity forces balance each other, the bottom-hole pressure of CO_2 is assumed to be close to that of point *A* (although in practice, the downhole temperature of CO_2 will be slightly higher due to heat conduction from the well, and CO_2 will most likely be in two phase regime). Isenthalpic expansion of CO_2 from 100 bar to a reservoir pressure of 20 bar (point *D*) reduces the CO_2 temperature to -10ºC. In general, for reservoirs with pressures lower than 35 bar J-T cooling effect reduces the CO_2 temperature to sub-zero values, as illustrated in Fig. 1. This can potentially lead to the formation of hydrates and freezing of pore water, as implied from the pressure-temperature diagram of the water/CO_2 system in Fig. 2a. The near-wellbore appearance of hydrates or ice can in turn result in the impairment of well injectivity and/or loss of well-related containment (Vilarrasa & Rutqvist, 2017). Moreover, the thermal stress generated by the cooling effect can lead to fracturing of the rock, the extent of which needs further investigation. An alternative solution will be to heat CO_2 before injection (path *A→B→C* in Fig. 1); however, this method is energy (and CO_2) intensive and adds further to the cost of CO_2 storage. Injection of CO_2 in gas form is also not desirable because storing similar mass rates of CO_2 require the drilling of multiple wells and requires a larger pore space.
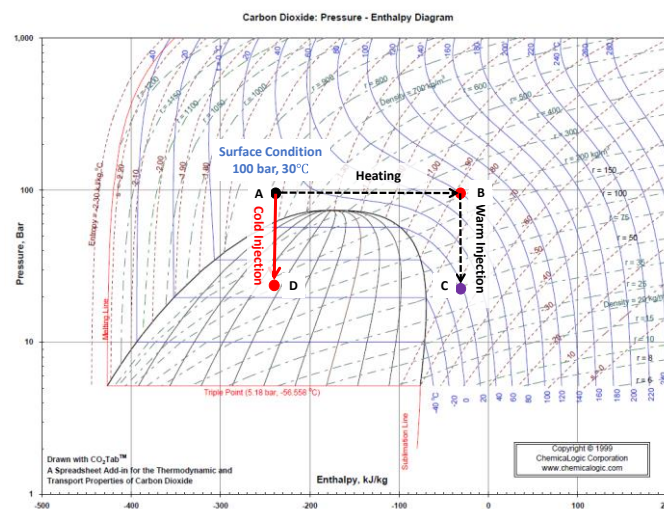

Fig. 1. Pressure-Enthalpy diagram of CO_2. The blue colours are the temperature contours.

The long-term and safe storage of CO_2 requires a detailed understanding of the physical, chemical, geo-mechanical and thermal effects caused by the injection of CO_2 in the reservoirs. This includes mobilisation of fines by CO2-water menisci (Chequer et al., 2020) , salinity alteration (Othman et al., 2019; Parvan et al., 2021; Yu et al., 2018) hydrate formation (Machado et al., 2023) and salt precipitation (Miri et al., 2015; Moghadasi et al., 2004). In addition, to identify the type of risk associated with cold CO_2 injection and design a mitigation plan, it is crucial to

quantify the range of expected temperatures in the depleted gas reservoirs. Oldenburg (2007) found that for a constant injection rate, lower permeability and higher porosity increase the effect of J-T cooling.

Mathias et al. (2010) derived an exact solution for CO_2 injection accounting for J-T cooling into an adiabatic reservoir (ignoring heat exchange with surrounding formations). The analytical model presented in his paper provides explicit formulae for the temperature and pressure profiles, and position of the cold front and quantifies the impact of several parameters on the cooling effect. This model, like all analytical models, allows for fast calculations for multivariant sensitivity studies and can benchmark the numerical methods for more complex modelling (Kacimov & Obnosov, 2023a, 2023b; Katzourakis & Chrysikopoulos, 2019; Moreno et al., 2021). These advantages explain numerous studies on the analytical modelling of problems related to CO_2 storage (Ahmadi & Chen, 2019; Celia et al., 2011; Moreno et al., 2021; Ziv Moreno & Avinoam Rabinovich, 2021; Z. Moreno & A. Rabinovich, 2021; Nguyen et al., 2022; Norouzi et al., 2022).

Heat exchange between the reservoir and the adjacent layers can significantly affect the non-isothermal flow in porous media (Bedrikovetsky, 1993; Lawal, 2020). Nevertheless, an exact solution for CO_2 injection into low-pressure reservoirs or aquifer accounting for this effect is not available. This paper drives an exact solution accounting for heat exchange between the reservoir and adjacent layers.

The explicit formula allows studying the timely evolution of the temperature profile, including the temperature penetration depth. The solution shows that the temperature profile stabilises with time and the penetration front stops. The solution also allows for calculating the well pressure at the injection well or well injectivity index and the dynamics of the heat penetration depth The explicit formulae for temperature and pressure allow calculating maximum injection rate that avoid formation of hydrates, i.e. the path well-reservoir in phase diagram does not enter the hydrate domain (Fig. 2). The validity of the model with Newton's law for heat exchange is determined by comparison with the exact solution.

The structure of the paper is as follows. Section 2 describes the major model assumptions and presents the mathematical model and the ensuing equations. Section 3 presents the explicit solution of the model, derived in Appendix A. Section 4 provides the calculation for the area of validity of the steady-state heat exchange model. Appendix B presents the exact solution for heat flux in adjacent layers and derives the criterion used to establish the domain of validity for the steady-state heat exchange term used in this paper. Section 5 presents the results of the

analytical model. Section 6 discusses the sensitivity study of the model, introducing the impact of dimensionless parameters on the temperature.
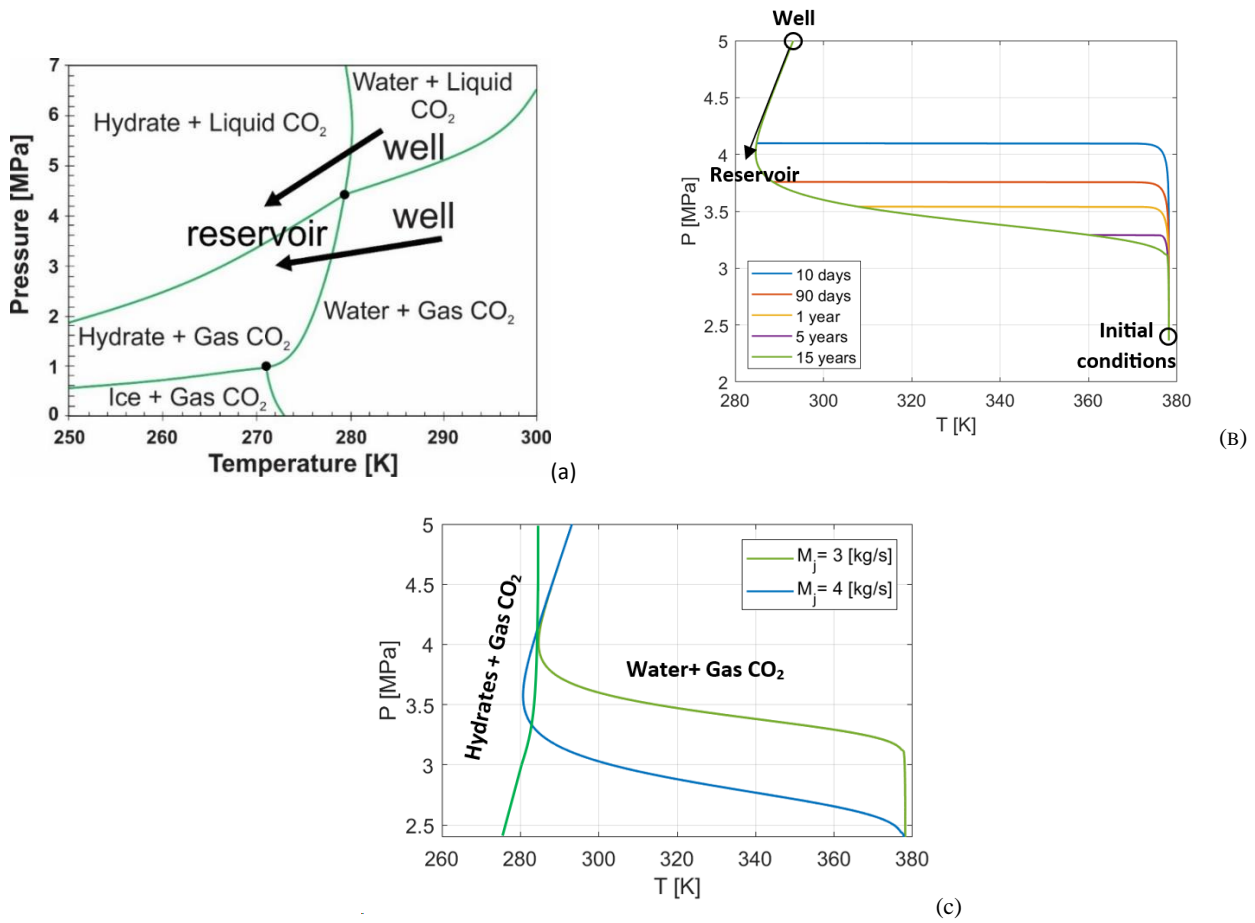

Fig. 2. (a) Pressure-Temperature phase diagram of water-CO_2 binary system, reproduced from Voronov et al. (2016), (b) (P,T) diagram based on our model. (c) Mass injection rate effect on a (P,T) diagram, at time $t_D = 5.4$.

2. MATHEMATICAL MODEL

This section presents the mathematical model for temperature profile evolution during CO_2 injection: the model assumptions (section 2.1) and derivation of the heat-transfer equation (section 2.2).

2.1 Model Assumptions

The main assumptions of the model are: (i) 1D radial unsteady-state single-phase non-isothermal flow in an infinite homogeneous reservoir; (ii) water, CO_2, and rock are incompressible; (iii) the reservoir (with permeability k [L^2] and porosity ϕ) contains water with an initial water saturation $S=1$; piston-like displacement of water by CO_2 resides constant saturation S_{wi} of immobile water behind the displacement front; (iv) temperature at outer boundaries of under and overburden shales is equal to initial temperature T_I [K]; (v) the temperature of the injected CO_2 in the wellbore is constant T_J [K]; (vi) Joule-Thomson coefficient, permeability, porosity, heat conductivity and heat capacity of rock and fluid are constant; (vii) CO_2 is injected at a constant rate of q_J [M^3T^{-1}], and pressure at drainage

radius is constant; (viii) water evaporation into gaseous phase is neglected; (ix) density and viscosity of fluids are constant; (x) heat exchange between surrounding shales and the reservoir occurs under steady-state conditions.

The model assumes steady-state heat exchange between the reservoir and the surrounding formations (Newton's law) $2\pi r \gamma^s l^{-1}(T - T_I)$ (Jang et al., 2022). So, the reservoir is bounded by overburden and underburden shales with thickness l [L]. Here, r [L] is the radial distance from the injection well, $T(r, t)$ [K] is the fluid temperature in the reservoir, γ^s [MLT^{-3}K^{-1}] is the heat-transfer coefficient (or overall thermal conductivity) of the seal in contact with CO_2, and T_I [K] is the initial temperature of the reservoir. This assumption is valid when the reservoir is hydrodynamically separated above and below from the adjacent layers by the impermeable seals. The heat fluxes behind and ahead of the horizontal boundary between the adjacent formations and seals are assumed equal. Heat flux is a product of thermal conductivity and temperature gradient. The thermal conductivity of an impermeable seal, e.g., shale is determined by that of the solid matrix, which is significantly lower than the thermal conductivity of the water residing in the adjacent permeable formation and forming a conductive cluster. Therefore, the temperature gradient in shales is expected to be significantly lower than the temperature gradient in the adjacent formation. This supports the assumption that the temperature at the upper and lower bounds of the adjacent shales layers remains equal to the initial temperature T_I.

Newton's law for the heat exchange between the reservoir and the adjacent layers is a commonly-used assumption for 1D non-isothermal flows in porous media (Atkinson & Ramey, 1977; Batycky & Brenner, 1997; Fedorov & Sharafutdinov, 1989; Gordeev et al., 1987; Jang et al., 2022; LaForce et al., 2014; Muradov & Davies, 2012; Muradov & Davies, 2009; Payne & Straughan, 1998; Pires et al., 2006; Xu et al., 2013; Yortsos & Gavalas, 1982; Zazovskii, 1983; Zolotukhin, 1979). However, the physical-geological conditions for Newton's law validity are not present in the literature. Derivations in Appendix B present the dimensionless criteria determining the validity of Newton's law. Furthermore, it is assumed that the heat exchange between the injected CO_2, water, and the rock occurs instantly. The heat transfer due to conduction in the flow direction is ignored compared to advection. The schematic of the radial problem for CO_2 injection into a depleted reservoir is given in Fig. 3.
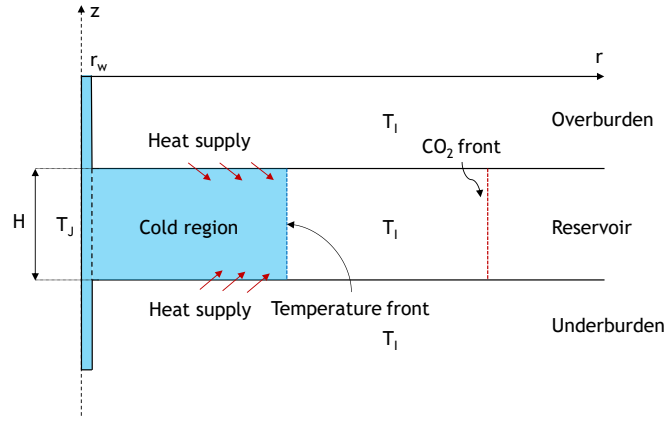
Fig. 3. Schematic of CO₂ injection into a depleted reservoir. The cold part (due to Joule-Thomson cooling effect) is shown in blue.

2.2 1-D Flow Equations

The energy-balance equation consists of the accumulation term of heat in the rock, CO_2, and water, advective heat transport, the J-T effect, and heat exchange of the reservoir with the adjacent layers (Lake et al. 2014; Wang 2022; Hashish & Zeidouni 2022):

$$2\pi r H \frac{\partial}{\partial t}\left\{\left[\phi(1-S_{wi})\rho_f c_f + \phi S_{wi}\rho_w c_w + (1-\phi)\rho_s c_s\right]T\right\} + q_J \rho_f c_f \left[\frac{\partial T}{\partial r} - \alpha_{JT}\frac{\partial p}{\partial r}\right] = -2\pi r \frac{\gamma^s}{l}(T-T_I) \qquad (1)$$

where ρ_f [ML⁻³] is density of CO_2, c_f [L²T⁻²K⁻¹] is the specific heat capacity of CO_2, ρ_w [ML⁻³] is the density of water, c_w [L²T⁻²K⁻¹] is the specific heat capacity of water, ρ_s [ML⁻³] is the rock density, c_s [L²T⁻²K⁻¹] is the rock specific heat capacity, q_J [L³T⁻¹] is the injection flow rate, H [L] is the formation thickness, α_{JT} [M⁻¹LT²K] is the J-T coefficient, and p [ML⁻¹T⁻²] is the fluid pressure. The unknown in Eq. (1) is the reservoir temperature $T(r,t)$.

The J-T coefficient of CO_2, α_{JT}, depends on the pressure and temperature as shown in Fig. 4. For the depleted reservoirs with pressures of less than 5 MPa, α_{JT} increases with a decreasing temperature. For a fixed temperature, α_{JT} can be assumed independent of pressure for these reservoirs, even though for larger pressures α_{JT} decreases with increasing pressure.

The overall heat transfer coefficient κ [MT⁻³K⁻¹] is defined as (Lawal, 2020):

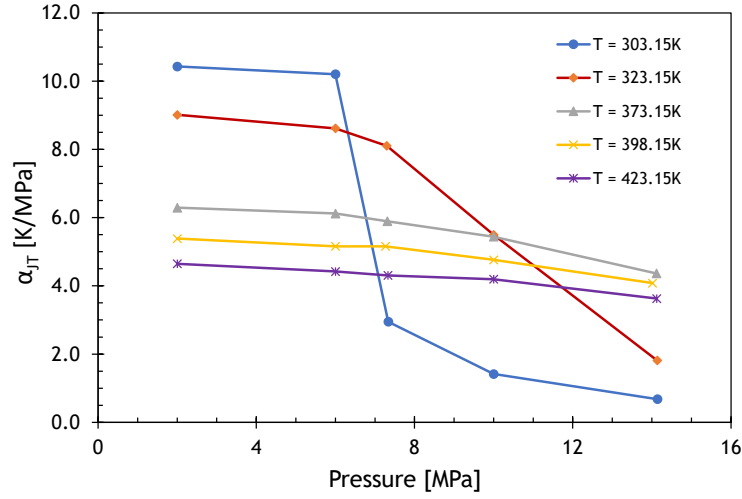$$\kappa = \gamma^s l^{-1} \qquad (2)$$

Fig. 4. Joule-Thomson coefficient of CO_2 as a function of pressure for different temperatures (modified from Gao et al. (2021))

It has been experimentally observed that when a fluid with a different temperature than the temperature of the porous medium is injected the heat loss (or gain) per unit length is almost constant. Consequently, the overall heat transfer coefficient, κ, is assumed constant in this study. In other words, the heat conductivity in the z-direction is assumed to be very large, which results in a constant temperature across the vertical thickness of the reservoir (LaForce et al., 2014). However, κ may vary with injection rate, the surface area in contact with surroundings, time, thermal conductivity of the surrounding porous medium, and/or the heat capacity of the reservoir, and the type of process (cold or hot fluid injection) (LaForce et al., 2014). Cold CO_2 injection into a reservoir filled with a hot fluid is analogous to cold water injection in geothermal reservoirs. The experimental data show that for cold water injection lower injection rates are more advantageous for heat extraction from the surrounding rocks.

The volumetric injection rate, q_J, is defined as:

$$q_J = M_J \rho_f^{-1} \tag{3}$$

where M_J [MT^{-1}] is the mass injection rate. The position of the CO_2 front r_f [L] is calculated assuming gas incompressibility:

$$M_J t = \pi \left(r_f^2(t) - r_w^2 \right)(1 - S_{wi}) \phi H \rho_f \tag{4}$$

$$r_f = \left(r_w^2 + \frac{M_J}{\pi \phi H \rho_f (1 - S_{wi})} t \right)^{1/2} \tag{5}$$

The pressure gradient in the reservoir is calculated using Darcy's law:

$$\frac{\partial p}{\partial r} = -\frac{\mu_f q_J}{2\pi r H k_{rf}^e k} \tag{6}$$

where μ_f [ML^{-1}T^{-1}] is viscosity of CO_2, and k_{rf}^e is the end-point relative permeability of CO_2. Finally, the substitution of Eq. (6) into Eq. (1) yields the first order partial differential equation:

$$\frac{\partial}{\partial t}\left\{\left[\phi(1-S_{wi})\rho_f c_f + \phi S_{wi}\rho_w c_w + (1-\phi)\rho_s c_s\right]T\right\} + \frac{q_J\rho_f c_f}{2\pi r H}\frac{\partial T}{\partial r} + \alpha_{JT}\frac{\mu_f\rho_f c_f q_J{}^2}{4\pi^2 r^2 H^2 k_{rf}^e k} = -\frac{\kappa}{H}(T-T_I) \tag{7}$$

The boundary condition (BC) correspond to the injection of CO_2 with a constant pressure and temperature:

$$r = r_w: \quad T = T_J, \quad p = p_J \tag{8}$$

where r_w [L] is the well radius.

The initial condition (IC) corresponds to the equality of the initial temperatures of the main reservoir rock and the adjacent layers, i.e.,

$$t = 0: \ T = T_I \tag{9}$$

The following dimensionless variables are introduced to nondimensionalize Eq. (7).

$$t_D = \frac{\gamma^s t}{H l c^{res}}, \quad r_D = \frac{r}{r_w}, \ T_D = \frac{T}{T_I} \tag{10}$$

Further, the dimensionless constants V^* and A^* are defined as:

$$V^* = \frac{q_J\rho_f c_f l}{2\pi r_w{}^2\gamma^s} \tag{11}$$

$$A^* = V^*\frac{\alpha_{JT}\mu_f q_J}{2\pi k_{rf}^e kHT_I} \tag{12}$$

By substituting Eqs. (10-12), the dimensional equation Eq. (7) transforms into the dimensionless form:

$$\frac{\partial T_D}{\partial t_D} + V^*\frac{1}{r_D}\frac{\partial T_D}{\partial r_D} = -A^*\frac{1}{r_D{}^2} - (T_{r,D}-1) \tag{13}$$

Additionally, the BC Eq. (8) and IC Eq. (9) are also expressed in dimensionless form as:

$$t_D = 0: T_D = 1 \tag{14}$$

$$r_D = 1: T_D = \frac{T_J}{T_I} \tag{15}$$

It is assumed that the heat transfer within the rock occurs instantaneously, i.e., the injected cold CO_2 is instantly heated up by the residing water and rock. This implies that the temperature front lags significantly behind the CO_2 front inside the reservoir.

3. EXACT ANALYTICAL SOLUTION

The exact solution of Eq. (13) with initial and boundary conditions Eqs. (14-15) is obtained by the method of characteristics (Boyce & DiPrima, 2013; Polyanin & Zaitsev, 2003) derived in Appendix A. The substitution of the dimensionless parameters given by Eqs. (10-12) into Eq. (A16) yields the dimensional form of the solution as:

$$T(r,t) = \begin{cases} T_I + (T_J - T_I)e^{-\frac{B}{V}\pi(r^2 - r_w^2)} + \frac{\alpha_{JT}\mu_f q_J}{4\pi k_{rf}^e kH}\left[Ei\left(\frac{B}{V}\pi r_w^2\right) - Ei\left(\frac{B}{V}\pi r^2\right)\right]e^{-\frac{B}{V}\pi r^2}; & \pi r^2 < \pi r_w^2 + V q_J t \\ \\ T_I + \frac{\alpha_{JT}\mu_f q_J}{4\pi k_{rf}^e kH}\left\{Ei\left(\frac{B}{V}\left(\pi r^2 - V q_J t\right)\right) - Ei\left(\frac{B}{V}\pi r^2\right)\right\}e^{-\frac{B}{V}\pi r^2}; & \pi r^2 > \pi r_w^2 + V q_J t \end{cases} \quad (16)$$

Here, the dimensional constants V and B are:

$$V = \frac{\rho_f c_f}{H[\varphi(1 - S_{wi})\rho_f c_f + \varphi S_{wi}\rho_w c_w + (1 - \varphi)\rho_s c_s]} \quad (17)$$

$$B = \frac{\kappa}{q_J H[\varphi(1 - S_{wi})\rho_f c_f + \varphi S_{wi}\rho_w c_w + (1 - \varphi)\rho_s c_s]} \quad (18)$$

The analytical model (A16), (16) can be extended for the case where the injected temperature changes with time – $T_J(t_D)$. In this case, T_J in Eq. (A16) must be substituted by $T_J(t_D-(r_D{}^2-1)/2V^*)$.

Let us define the depth of temperature wave penetration as a coordinate of the "centre" of the wave. For variable r, the probability distribution function can be defined as:

$$F(r) = \frac{(T(r,t) - T_I)r}{\int_{r_w}^{\infty}(T(r,t) - T_I)r\,dr} \quad (19)$$

The arithmetic mean of r is

$$r_p = \int_{r_w}^{\infty}F(r)r\,dr = \frac{\int_{r_w}^{\infty}(T(r,t) - T_I)r^2\,dr}{\int_{r_w}^{\infty}(T(r,t) - T_I)r\,dr} \quad (20)$$

4. AREA OF VALIDITY OF THE MODEL

This section determines the area of validity of the analytical model, including comparison between the solutions for adiabatic and non-adiabatic reservoirs (section 4.1), formulation of the method of 1D model validation by

comparison with 2D solution (section 4.2), and calculations of validity intervals for the model parameters and independent variables (section 4.3).

4.1 Definition of the Basic Case for Sensitivity and Model Validation

To validate the developed analytical model, the solution given by Eq. (19) was compared with the results of Mathias et al. (2010) in the limit of no heat transfer between the reservoir and the adjacent layers, i.e., $\kappa \rightarrow 0$. The parameters provided in Table 1 are used as a basic case for all calculations in this paper. Table 2 presents the intervals of variation of variables. Fig. 5 shows the close agreement between the numerical implementations of two models. The time intervals in Fig. 5 correspond to dimensionless time, $t_D = 0.01, 0.02, 0.09, 0.3, 1.8, 5.4, 7.1$.

As expected, the temperature front falls behind the CO_2 front because of the heat provided by the rock (the volumetric heat capacity of the rock is much larger than those of both water and CO_2). The temperature decreases from injection temperature to a minimum value and then sharply increases to the initial temperature of the reservoir. There are two distinctive features for the solution of the case, where $\kappa \rightarrow 0$: (1) temperature decreases to a minimum value just upstream of the sharp front at each timestep, and (2) the temperature front keeps moving inside the reservoir for as long as CO_2 injection continues. The sharp increase to the initial temperature (shock front) is due to absence of conduction in the analytical model. In accordance with the properties of the radial flow (i.e., large pressure drops near the injection point), the cold front penetrates quickly inside the reservoir. If the injected CO_2 is undersaturated, the residing water in the pores evaporates; and therefore, the water saturation reduces to near-zero close to the injection well. However, the speed of the temperature front is expected to be larger than that of the drying front such that a region with a non-zero water saturation appears between the dry-out and cold fronts in a relatively short time after injection of CO_2. This is schematically shown in Fig. 6. If the pressure and temperature fall within in the hydrate region on the CO_2/water phase diagram in Fig. 2, CO_2 hydrates might form potentially leading to blockage of CO_2 flow.
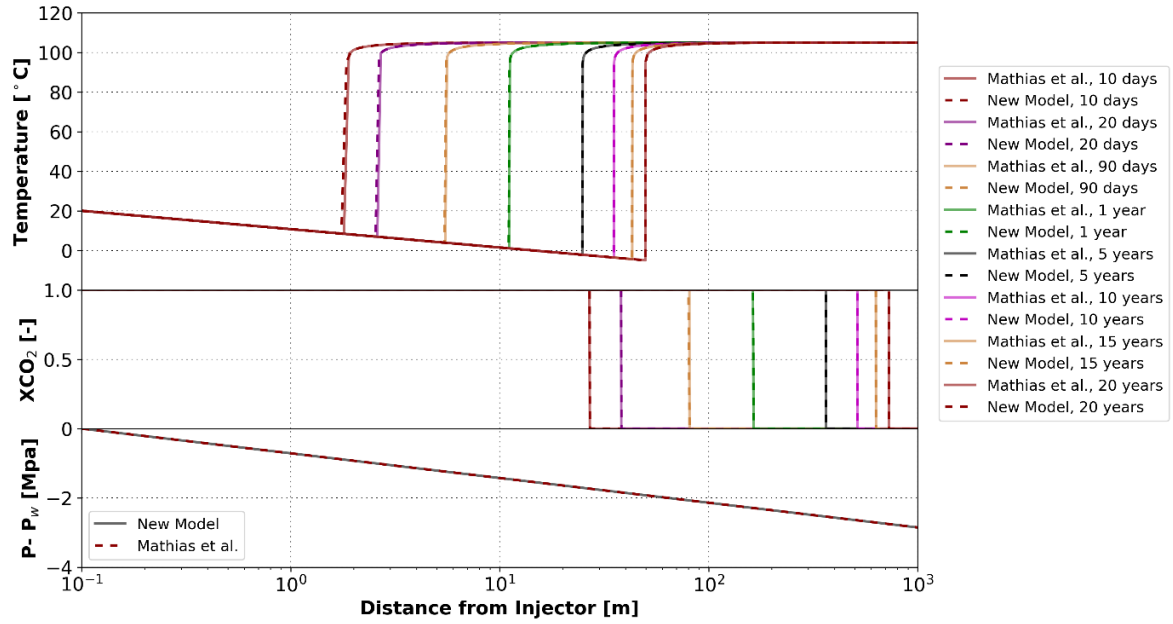
Fig. 5. Comparison of the results of the current model with Mathias et al. (2010) model ($\kappa = 0$).

Table 1. Model parameters used in this study.

Parameter	Symbol	Unit	Value
Formation thickness	H	m	91
Porosity	ϕ	[-]	0.11
Permeability	k	m^2	2×10^{-15}
End point relative permeability	k_{rf}^e	[-]	1
Well radius	r_w	m	0.1
Rock density	ρ_S	kg/m^3	2600
Water density	ρ_w	kg/m^3	992
CO$_2$ density	ρ_f	kg/m^3	141.4
CO$_2$ viscosity	μ_f	Pa.s	16.7×10^{-5}
Heat capacity of rock	c_S	J/kg/K	1000
Heat capacity of water	c_w	J/kg/K	4037
Heat capacity of CO$_2$	c_f	J/kg/K	904
Joule Thomson coefficient	α_{JT}	K/Pa	10.2×10^{-6}
Reservoir pressure	p_w	Pa	50×10^5
Reservoir temperature	T_I	K	378.15

14

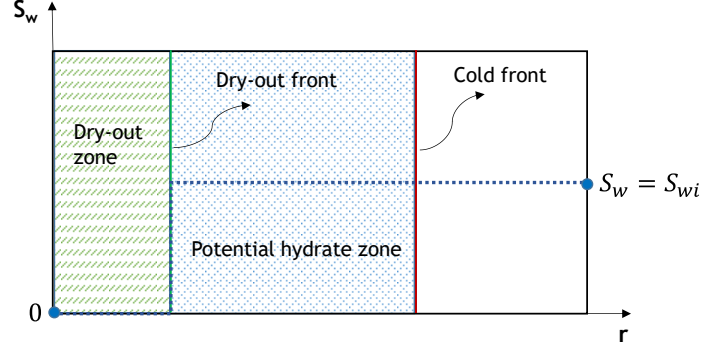|				
Injection temperature	T_J	K	293.15	
CO_2 mass injection rate	M_J	kg/s	3	
Connate water saturation	S_{wi}	[-]	0.2	

Fig. 6. Formation of a region with a non-zero water saturation between dry-out and cold fronts.

4.2 Formulating the Criterion for Validity of the Heat Exchange Term.

The primary assumption of the model given by Eq. (1) is steady state heat exchange between surrounding formations and impermeable shale that confines the reservoir, which is the Newton's law. This section establishes the domain of validity for the heat exchange term used in the energy balance (Eq. (1)), aiming to determine the condition under which the discrepancy between the temperature at the interface, $\theta(z_D = 0, t_D)$, and the initial reservoir temperature, $T = T_I \rightarrow \theta = 1$, is considered insignificant. In our case, we constrain the discrepancy between the two solutions for temperature to the difference of less than or equal to 10%.

We utilize the solutions obtained in Appendix B for the temperature profile at the interface between adjacent impermeable shale, as derived in Eq. (B19). The condition in dimensionless variables is as follows:

$$1 - \theta(z_D = 0, t_D) < \varepsilon, \quad \varepsilon = 0.1 \tag{21}$$

In this analysis we introduce two dimensionless constants, A^* and V^* given in Eq. (11) and Eq. (12). Also, we present the constant ω determined in Appendix B as Eq. (B9):

$$\omega = \sqrt{\frac{c^{res}\gamma^s H}{c^a \gamma^a l}} \tag{22}$$

Newton's law is valid when the temperature on the outer bounds of the adjacent seals is equal to the initial reservoir temperature. This condition depends on conductivity and capacity of the adjacent formation layers i.e., depends on

the heat conductivity (γ^a) and volumetric heat capacity (c^a). Indeed, equality of the temperature on the outer shale bounds to initial reservoir temperature corresponds to ω tending to zero.

The intervals for parameters A^*, V^* and ω are determined from typical fluid and rock properties. The details below highlight the values adopted in this work. The heat capacities of gas, water and rock varying from 709 J (kg K)$^{-1}$ to 1476 J (kg K)$^{-1}$, 3965 J (kg K)$^{-1}$ to 4335 J (kg K)$^{-1}$ and from 776 J (kg K)$^{-1}$ to 1215 J (kg K)$^{-1}$, respectively. The heat conductivities of shale and adjacent formations ranges from 1 W (m K)$^{-1}$ to 3.7 W (m K)$^{-1}$ and from 3.7 W (m K)$^{-1}$ to 5 W (m K)$^{-1}$, respectively. The densities of gas, water and rock vary from 0.5 kg m^{-3} to 1236 kg m^{-3}, from 527 kg m^{-3} to 1000 kg m^{-3} and from 2270 kg m^{-3} to 3200 kg m^{-3}, respectively. In addition, the thickness of the reservoir and the shale vary from 1 m to 100 m and from 1 m to 3.33 m, respectively. Well radius varies from 0.05 m to 0.13 m. Injection rate varies from 0.005 m^3 s^{-1} to 0.04 m^3 s^{-1}. J-T coefficient varies from 7×10^{-6} K/Pa to 1.1×10^{-5} K/Pa. Additionally, CO_2 viscosity varies from 1.1×10^{-5} Pa s to 2.7×10^{-4} Pa s. Permeability varies from 3.9×10^{-16} m^2 to 5.9×10^{-14} m^2. Finally, porosity varies from 0.1 to 0.3 and connate water saturation varies from 0.2 to 0.4.

Given that our solution in Eq. (B19) is notably influenced by system parameters- A^*, V^* and ω, a domain made of the three dimensionless constants, (A^*, V^*, ω) in Eq. (B19) is established. The eight vertices of the tetrahedron represented by dots in Fig. 7 correspond to the extreme values of A^*, V^* and ω. The inner dot numbered 9 corresponds to the unperturbed base case given in Table 1**Error! Reference source not found.**.

Fig. 7. A tetrahedron defining the domain of the three dimensionless constants in the system.

Table 2 summarizes the critical values of the 9 coordinate points illustrated in Fig. 7.

Table 2. Critical points of the (A^*, V^*, ω) domain

Vertices	V^*	A^*	ω
1	4.51	1.08×10^{-4}	1.56×10^{-1}
2	4.51	2.14×10^{3}	1.56×10^{-1}

3	4.51	2.14×10^3	1.48×10^1
4	4.51	1.08×10^{-4}	1.48×10^1
5	1.55×10^7	1.08×10^{-4}	1.56×10^{-1}
6	1.55×10^7	2.14×10^3	1.56×10^{-1}
7	1.55×10^7	2.14×10^3	1.48×10^1
8	1.55×10^7	1.08×10^{-4}	1.48×10^1
9	1.63×10^4	1.28×10^2	9.29

4.3 Determining the Area of Validity

Our aim is to determine a region of validity where the condition in Eq. (21) is upheld. To visualize this, we plot $1 - \theta(z_D = 0, t_D)$ against dimensionless time for various radial distances in the reservoir in Fig 8a. We also obtain a generalized area of validity in the (r_D, t_D) plane in Fig 8b, where r_c is the critical radius.

(a)   (b)
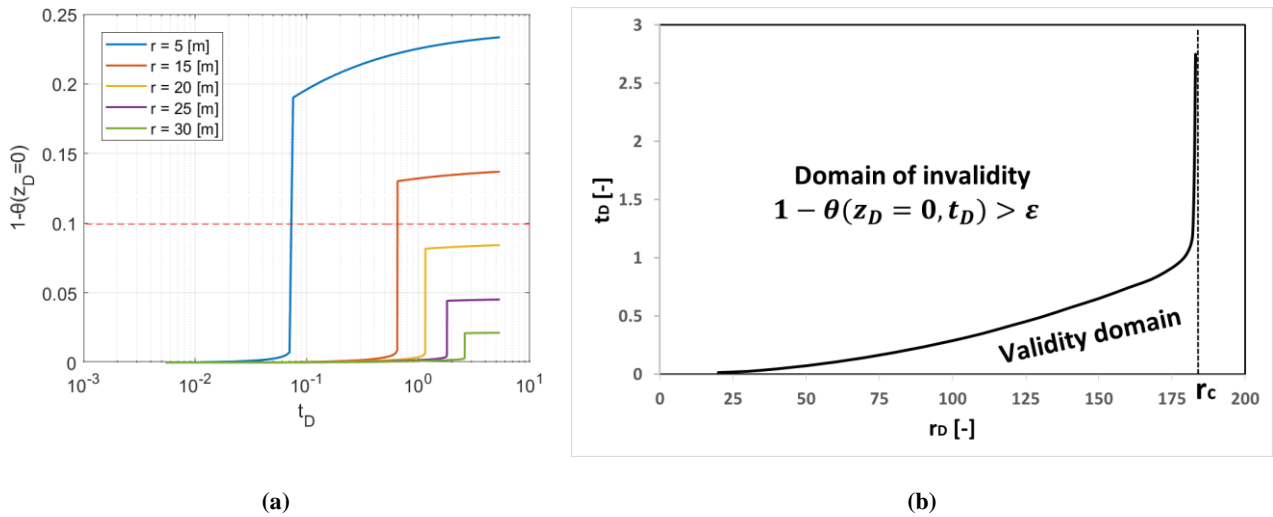
Fig 8. Validity of steady state heat exchange (a) validity vs. time for different radii. (b) domain of validity

To explore the scope of the area of validity, we show the impact of five typical values of ω, at a constant radial distance of $r = 5$ m, in Fig. 9.
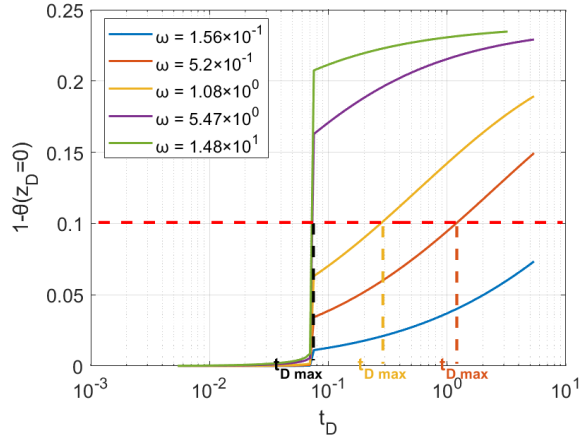
Fig. 9. Newton's law criterion vs. time, for different ω values. Plotted for $r = 5$ m.

The 10% error dashed line in Fig 8a and Fig. 9 indicates our chosen criterion for Newton's law, i.e., $1 - \theta(z_D = 0, t_D) < 0.1$. In case a different criterion is needed, the area of validity for Newton's law changes accordingly. To provide an analysis on the validity in each of the points presented in Table 2, we introduce the definition for radius of injection, following Eq. (5):

$$r_{inj} = \sqrt{\frac{M_J}{\pi \phi H \rho_f (1 - S_{wi})} t_{inj}} \tag{23}$$

Here, t_{inj}[T] is the time of injection. Considering $t_{inj} = 10$ years, we plot $1 - \theta(z_D = 0, t_D)$ for each point in Table 2 under the constraint of the chosen 10% error margin. The plots in Fig 8a show that for short distances near the well ($r = 5$ m , $r = 15$m) validity of the model based on Newton's law is limited. Newton's law is obeyed until the moment of arrival of temperature front to these near wellbore points, beyond which invalidity ensues. However, for larger distances away from the wellbore, the solution is valid for the overall time domain. The domain of validity is further shown in Fig 8b. There exists such a critical radius (r_c) beyond which the solution is valid for all times.
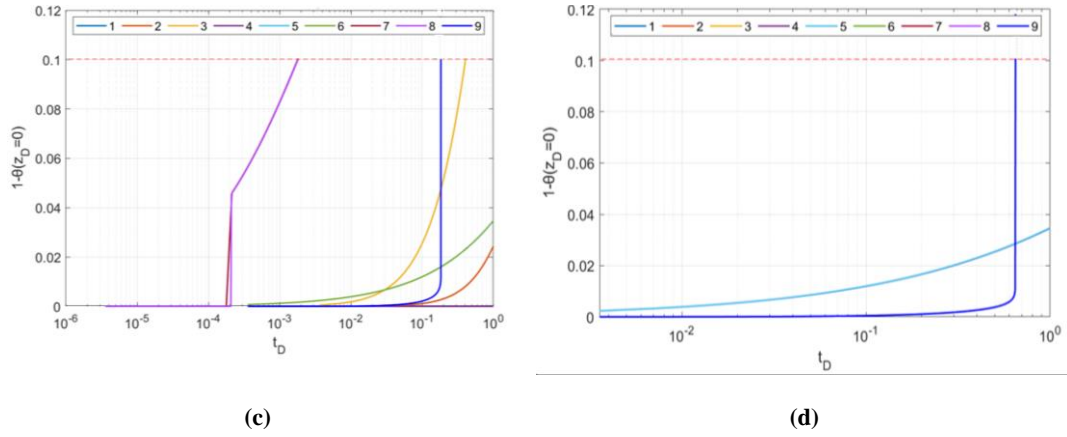

(a)

(b)
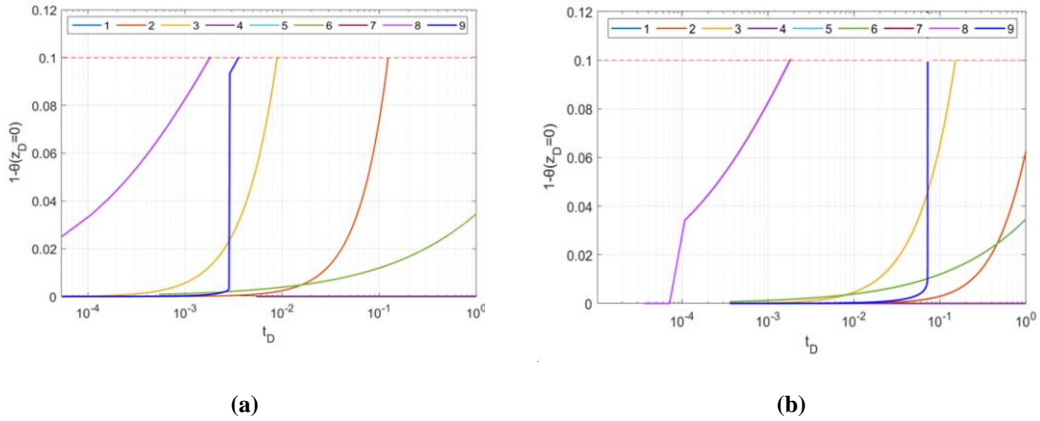
Fig. 10. Difference between temperature on the outer bounds of shale and initial reservoir temperature, to validate Newton's law, temperature history at the distance from injectors at (a) $r = 0.002\ r_{inj}$, (b) $r = 0.01\ r_{inj}$, (c) $r = 0.015\ r_{inj}$, (d) $r = 0.03\ r_{inj}$

5. RESULTS OF THE ANALYTICAL MODELLING

This section presents the results of the derived analytical model and discusses their relevance for CO_2 storage in the low-pressure or depleted fields. The impact of heat exchange between the main formation and the surrounding rock on the propagation of the temperature front is shown in Fig. 11. A heat transfer coefficient of $\kappa = 2.5$ W/m²/K was used in the calculations (Cermak & Rybach, 1982; Labus & Labus, 2018; Robertson, 1988; Schoen, 2015). For the purpose of comparison, Fig. 11 further shows the case of no heat exchange ($\kappa \to 0$) with the dashed curves. Initially and for relatively short times, the impact of the heat gain from the surrounding layers is not significant.
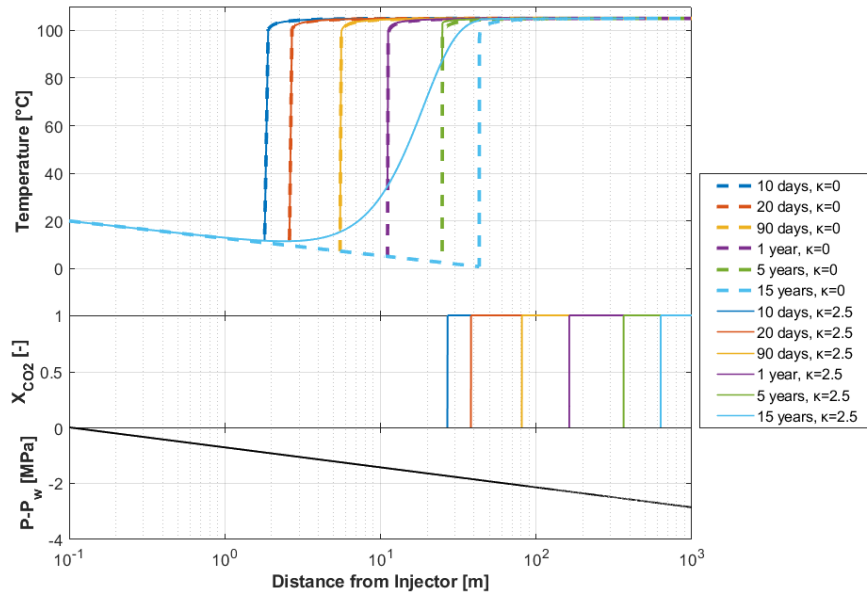
Fig. 11. The impact of heat exchange on temperature profile (solid lines) in comparison to adiabatic system (dashed lines), CO_2 front position and Pressure drop for varying times.

However, as CO_2 injection continues, the heat supplied by these layers heats the injected CO_2 and therefore the temperature increases slightly before jumping to the initial temperature of the reservoir. Unlike the case with no heat exchange, the temperature upstream of the shock is not the lowest temperature. Indeed, a key difference is that the position and the value of the minimum temperature remains fixed for all times in the new model. The area between the solid and the dashed curves in Fig. 11 represents the extent of the impact of the heat exchange. The area increases with time and as a result the length of the shock front becomes smaller every timestep, until it disappears completely. This corresponds to the time at which the system reaches steady state, and the temperature front no longer moves. The solution of the ordinary differential equation (ODE) is obtained by the separation of variables:

$$T(r) = T_I + (T_J - T_I)e^{-C(\pi r^2 - \pi r_w^2)} + D[Ei(C\pi r_w^2) - Ei(C\pi r^2)]e^{-C\pi r^2} \tag{24}$$

Here, C and D are defined as follows:

$$C = \frac{\kappa}{q_J \rho_f c_f}, \quad D = \frac{\alpha_{JT} \mu_f q_J}{4\pi k_{rf}^e k} \tag{25}$$

The time intervals in Fig. 11 correspond to dimensionless timey, $t_D = 0.01, 0.09, 0.3, 1.8$, and 5.4, respectively. Eqs. (24) and (25) indicate that the position of the steady state temperature depends largely on the injection rate, the volumetric heat capacity of CO_2 and rock properties. The pressure profile under the assumptions of gas incompressibility and constant viscosity is steady state; it is obtained by integration of Eq. (6) with BC Eq. (8) for pressure. The temperature profile in Fig. 11 shows temperature decreases from the well to the temperature front, and then monotonically increases until initial temperature. Minimum temperature is achieved exactly behind the temperature front. It is crucial to determine a minimum injection rate at which the temperature behind the temperature front and pressure along the temperature front are not conducive for hydrate formation (as illustrated by the phase diagram in Fig. 2a). Additionally, Fig. 2b. shows the pressure-temperature path in the phase diagram, where the reservoir point corresponds to minimum temperature. The length of the segment, injection well-reservoir, as it follows from Eq. (6), is proportional to injection rate q_J. This allows determining the minimum rate of hydrate formation. Fig. 2c shows two solutions that corresponds to mass injection rates of $M_J = 3$ kg/s and $M_J = 4$ kg/s.

According to Fig. 2c, hydrates formation occurs when the plot crosses the Hydrates + Gas CO_2 phase boundary, which is evident only for the higher injection rate.

6. SENSITIVITY STUDY OF THE MODEL

This section investigates the sensitivity of the analytical model to the model parameters: heat transfer coefficient (subsection 6.1), permeability (subsection 6.2), and reservoir thickness as well as injection rate (subsection 6.3). Additionally, the effect of the dimensionless parameters $A*$ and $V*$ on the temperature profile is investigated in subsection 6.4.

6.1 Effect of Heat Transfer Coefficient

The impact of the heat transfer coefficient, κ, is shown in Fig. 12. With the increase of κ, a higher amount CO_2 is heated and therefore the cold front is retarded, compared to the case where κ is smaller. Moreover, the minimum temperature is slightly lower for the case with the smaller κ, as illustrated in Fig. 12a.

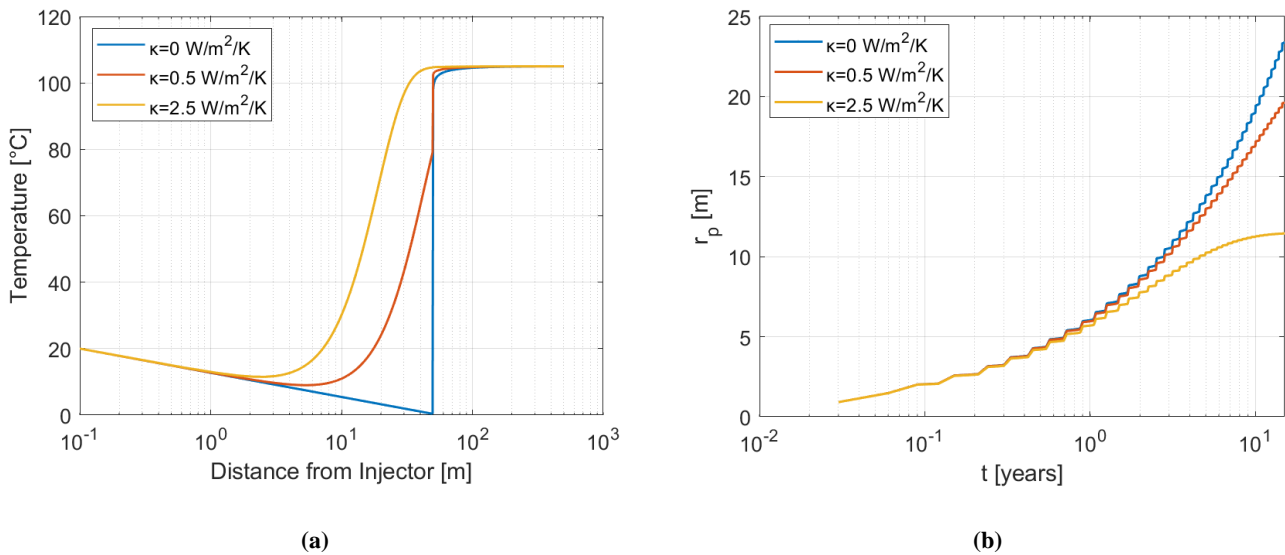(a)   (b)

Fig. 12. (a) The impact of the heat transfer coefficient, κ, on the temperature profile. (b). The impact of the heat transfer coefficient, κ, on the temperature penetration depth.

Fig. 12b shows that in the adiabatic reservoir, the penetration depth, which was introduced by Eq. (20), does not stabilize (blue curve). Stabilization of the heat penetration is achieved with the presence of heat exchange in the system. For the given temporal range, the curve corresponding to the lower value for heat conductivity does not stabilize, while the curve corresponding to the higher value achieves stabilization. The three values of heat conductivity presented in Fig. 12 correspond to the following dimensionless parameters- $(A*,V*\rightarrow\infty)$, $(A*=7.2\times10^2, V*=8.6\times10^4)$, $(A*=1.4\times10^2, V*=1.7\times10^4)$, respectively.

6.2 Effect of Permeability

Fig. 13 shows the sensitivity of the model to varying rock permeabilities. As stated earlier, the magnitude of temperature reduction due to the J-T effect depends on the pressure gradient and the J-T coefficient. For fixed injection pressure and flowrate at the boundary, the pressure gradient increases with decreasing reservoir permeability, causing an increased temperature drop. However, this conclusion is valid only when equal flowrates are considered for different permeabilities. For a heterogeneous reservoir, the injected CO_2 will be distributed in proportion to the permeability of each layer. If the permeability contrast is large, then the large fraction of CO_2 will flow through the high permeability layer causing a larger pressure drop compared to the low-permeability layer. Therefore, for heterogeneous reservoirs with large permeability contrast, the "isenthalpic" expansion of CO_2 will result in lower temperatures in the high permeability layers.

It is worth mentioning that when CO_2 becomes liquid or the pressure exceeds the critical pressure of CO_2 the magnitude of α_{JT} also reduces, especially in the colder regions near wellbore (see Fig. 4) resulting in lower cooling effects. Furthermore, the presence of impurities in the injected CO_2 or contamination of CO_2 with the gas already present in the reservoir will also affect the temperature drop and the extent of the cooling zone (Ziabakhsh-Ganji & Kooi, 2014). Gases like SO_2 expand the cooling zone while gases like N_2 and CH_4 tend to contract this zone (Ziabakhsh-Ganji & Kooi, 2014). The Joule-Thomson cooling effect is more pronounced at low-permeability and thin layers, assuming a constant injection rate. With the increase of the reservoir permeability or thickness the impact becomes less and after a certain value the steady-state temperature profile appears to be independent of these parameters.
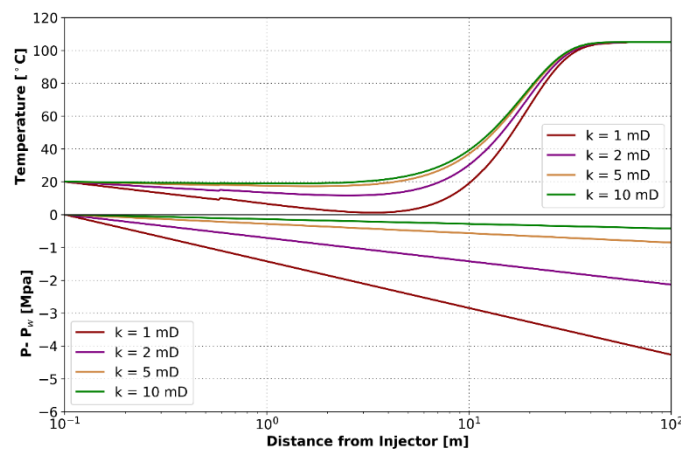

Fig. 13. The impact of permeability on the temperature profiles.

The four values of heat conductivity presented in Fig. 13 correspond to the following values of dimensionless parameter A^*: $A^*=2.8\times10^2$, $A^*=1.4\times10^2$, $A^*=5.7\times10^1$, $A^*=2.8\times10^1$, respectively.

6.3 Effect of System Parameters on Minimum Reservoir Temperature

In the sensitivity analysis shown in Fig. 14, only the investigated model parameter was changed while the other parameters remained constant. For simplicity the parameters are normalized to the parameters of the base-case presented in Table 1. Moreover, the r_{norm} on the y-axis is relative to the position of the steady-state temperature of the base case. The normalized distance has a near linear relationship with the mass injection rate, i.e., the higher the injection rate the longer the cold front travels inside the reservoir. In addition, the minimum temperature significantly decreases as the injection rate increases. For example, with doubling of M_J, the minimum temperature drops from 10 ºC to -10 ºC, which has huge implications for a CO_2 storage project.
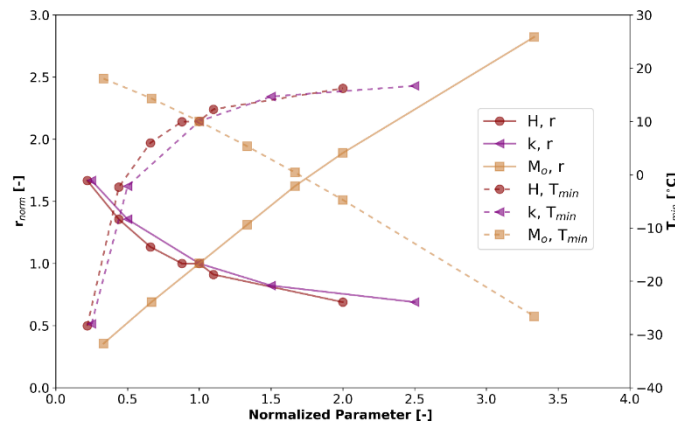

Fig. 14. The impacts of the mass injection, permeability and reservoir thickness on the minimum temperature and the steady-state position of the temperature front in the reservoir. The axes are normalized to the parameters of the base case.

6.4 Sensitivity to Change in the Dimensionless Constants

The dimensionless constants A^* and V^*, as defined in Eq. (11) and Eq. (12), are the parameters that account for the J-T effect, and the heat front velocity, respectively. An increase in parameter A^* is equivalent to an increase in the J-T coefficient, injection rate and shale thickness, as well as a decrease in reservoir thickness, shale heat conductivity and permeability. Also, an increase in parameter V^* corresponds to an increase in shale thickness and injection rate, as well as a decrease in shale conductivity.
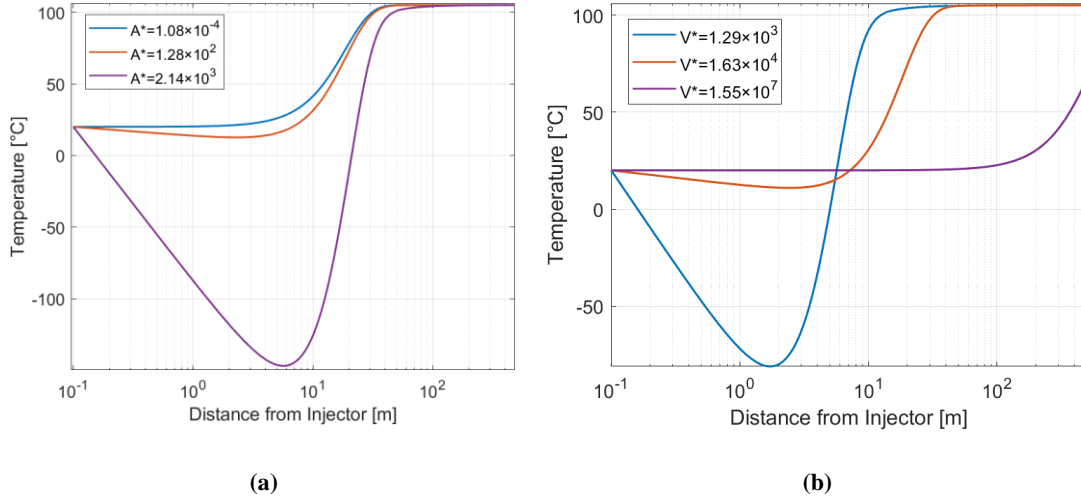
Fig. 15. Temperature profile sensitivity to (a) $A*$ parameter (b) $V*$ parameter, at time $t_D = 7.1$.

Fig. 15 show the sensitivity of the temperature profile to the dimensionless constants, $A*$ and $V*$. From Fig. 15a, it is observed that, while maintaining all other system parameters constant and varying $A*$, the temperature drop in the system ranges from $\Delta T = 170°C$ to $\Delta T = 0$. In Fig. 15b, varying the values of $V*$, while holding all other system parameters fixed results to temperature drops varies between $\Delta T = 95°C$ to $\Delta T = 0$. Hence, the system is more sensitive to modifications in parameter $A*$ when assessing the temperature profiles.

7. DISCUSSION

The analytical model presented in this paper (Eq. (19)) assumes a constant injection rate; under given pressure drawdown between the injector and the reservoir. Eq. (17) defines the dimensional parameter for heat front velocity. As temperature front moves significantly slower than the CO_2-water front; $V \ll 1$, for which water saturation in the cold region is only slightly above S_{wi}. However, varying two-phase mobility during the displacement can affect pressure behaviour, so well injectivity prediction requires accounting for the overall saturation profile. Self-similar solution for displacement of water by CO_2 can be matched with the analytical model (Eq. (19)).

Another mechanism requiring two-phase formulation during CO_2 injection, which is not accounted for in this study, is mobilisation and migration of natural reservoir fines, that are detached by gas-water menisci (Chequer et al., 2020; Nguyen et al., 2022). The governing system includes the equation for motion of gas-water interface, where fines detachment occurs (Shapiro, 2015). The detachment is determined by the interaction of capillary and DLVO forces exerting the attached fine particle (Yuan & Moghanloo, 2018; Yuan & Moghanloo, 2019). The saturation variation from 1 to S_{wi} around CO_2-water front requires generalisation of the overall unsteady-state model for two-

phase flow with moving interface (Shapiro, 2016, 2018). Accounting for two-phase flow with fines migration in the model Eq. (19) captures the effects of injectivity decline during CO_2 injection.

Other mechanisms contributing to formation damage and injectivity decline, triggered by J-T cooling effect, encompass salt precipitation, rock dissolution, mineral precipitation reaction, and hydrate formation (G Moghanloo et al., 2017; Ge et al., 2020; Nguyen et al., 2021; Turner et al., 2022). Adding those effects into Eq. (19) reflects the effects of formation damage on well injectivity during CO_2 storage in aquifers and depleted gas fields. The governing system includes balance equations for energy and mass of salt, methane, and chemical species. In large scale approximation, the hyperbolic system of the quasi-linear equations contains shocks of temperature, saturation, and component concentrations; the corresponding Riemann problems are self-similar (Lake, 1989; Polyanin et al., 2002; Polyanin & Zaitsev, 2003). Accounting for dissipative effects of diffusion and reaction kinetics induces the smoothening of the shocks by travelling wave solutions (Bedrikovetsky, 1993; Polianin & Dil′man, 1994). In several cases, the obtained analytical solutions for water displacement allow for exact and asymptotic upscaling (Cheng & Rabinovich, 2021; Rabinovich et al., 2015); numerous references for upscaling relevant to CO_2 injection are available from review (Bedrikovetsky & Borazjani, 2022). In addition, the analytical solution can be obtained for a temperature dependency of the J-T coefficient. This will introduce non-linear term $\alpha_{JT}(T)$ in Eq. (12). For this equation, the characteristics are straight lines. The solution along characteristics is obtained by separation of variables and is given by implicit integral in temperature.

Fig. 9 illustrates how the system parameter ω impacts the validity of Newton's law within the system. As ω decreases, the period during which Newton's law remains valid ($t_{D\ max}$) increases, and for the lowest value, there is no such time limit. In general, for every $\varepsilon \ll 1$, there does exist such δ and t_δ that for $t < t_\delta$, $T_I - T(z = 0, t) < \varepsilon$. Furthermore, Fig. 10 indicates that for injection processes with specific values for A^*, V^*, and ω, Newton's law holds over a longer observation period when the radius is larger.

8. CONCLUSIONS

This paper presents an analytical model for a 1D axi-symmetric problem, in which CO_2 is injected with constant rate and temperature into a semi-infinite porous medium saturated by gas and water. The model accounts for the Joule-Thomson effect due to "isenthalpic" expansion of the gas and quasi steady-state heat exchange - Newton's law - between the reservoir and the adjacent (over- and under-burden) layers. The exact solution leads to explicit expressions for the temperature profile. The solution shows that the temperature front lags significantly behind the

CO₂ front due to instant heat exchange between the rock, connate water, and CO_2. The exact solution ahead of the front depends on initial temperature and is independent of the injected temperature. In adiabatic reservoir without heat supply from the adjacent layers, the temperature decreases from the well to a minimum value on the heat front, then jumps up on front followed by slow increase up to the initial reservoir temperature. The heat supplied by the adjacent layers has two major impacts on the temperature profile: (1) it decelerates the penetration depth propagation, and (2) it decreases the temperature decline from the well to heat front. Also, the minimum temperature for this case is lower than at the case with no heat gain from the surrounding layers, and its position and value with time remain unchanged. We show that the Newton's heat-exchange law yields tending of the temperature profile to steady-state profile as time tends to infinity; the penetration depth position stabilises. The position of the steady-state temperature strongly depends on dimensionless Joule-Thomson number $A*$; the dimensionless heat front velocity $V*$ affects less. The results of this study have major implications for CO_2 storage in depleted gas fields and can be used as guide to quantify whether the temperature profile in the reservoir falls within the hydrate formation zone, or whether the induced temperature gradient can jeopardize the mechanical integrity of the rock.

10. REFERENCES

Ahmadi, M. A., & Chen, Z. (2019). Analytical Model for Leakage Detection in CO2 Sequestration in Deep Saline Aquifers: Application to ex Situ and in Situ CO2 Sequestration Processes. *ACS Omega*, *4*(25), 21381-21394. https://doi.org/10.1021/acsomega.9b02668

Atkinson, P. G., & Ramey, H. J., Jr. (1977). *Problems Of Heat Transfer In Porous Media* SPE Annual Fall Technical Conference and Exhibition, https://doi.org/10.2118/6792-MS

Battashi, M., Farajzadeh, R., Bimani, A., Al Abri, M., Mjeni, R., Karpan, V., Fadili, A., & van Wunnik, J. (2022). Insights into oil recovery mechanism by Nothing-Alternating-Polymer (NAP) concept. *Journal of Petroleum Science and Engineering*, *211*, 110114. https://doi.org/https://doi.org/10.1016/j.petrol.2022.110114

Batycky, R. P., & Brenner, H. (1997). Thermal macrotransport processes in porous media. A review. *Advances in Water Resources*, *20*(2), 95-110. https://doi.org/https://doi.org/10.1016/S0309-1708(97)89141-5

Bedrikovetsky, P. (1993). *Mathematical Theory of Oil & Gas Recovery*. https://doi.org/10.1007/978-94-017-2205-6

Bedrikovetsky, P., & Borazjani, S. (2022). Exact Solutions for Gravity-Segregated Flows in Porous Media. *Mathematics*, *10*(14).

Boyce, W. E., & DiPrima, R. C. (2013). *Elementary differential equations and boundary value problems* (10th ed.). John Wiley & Sons, Inc.

Celia, M. A., Nordbotten, J. M., Court, B., Dobossy, M., & Bachu, S. (2011). Field-scale application of a semi-analytical model for estimation of CO2 and brine leakage along old wells. *International Journal of Greenhouse Gas Control*, *5*(2), 257-269. https://doi.org/https://doi.org/10.1016/j.ijggc.2010.10.005

Cermak, V., & Rybach, L. (1982). Thermal Conductivity and Specific Heat of Minerals and Rocks. In (pp. 305–343). https://doi.org/10.1007/10201894_62

Cheng, K. B., & Rabinovich, A. (2021). Optimization-based upscaling for gravity segregation with 3D capillary heterogeneity effects. *Journal of Hydrology*, *603*, 127062. https://doi.org/https://doi.org/10.1016/j.jhydrol.2021.127062

Chequer, L., Bedrikovetsky, P., Badalyan, A., & Gitis, V. (2020). Water level and mobilisation of colloids in porous media. *Advances in Water Resources*, *143*, 103670. https://doi.org/https://doi.org/10.1016/j.advwatres.2020.103670

Fedorov, K. M., & Sharafutdinov, R. F. (1989). Contribution to the theory of nonisothermal flow through porous media with phase transitions. *Fluid Dynamics*, *24*(5), 721-727. https://doi.org/10.1007/BF01051725

G Moghanloo, R., Yan, X., Law, G., Roshani, S., Babb, G., & Herron, W. (2017). Challenges Associated with CO2 Sequestration and Hydrocarbon Recovery. In. https://doi.org/10.5772/67226

Gao, M., Wang, L., Chen, X., Wei, X., Liang, J., & Li, L. (2021). Joule–Thomson Effect on a CCS-Relevant (CO2 + N2) System. *ACS Omega*, *6*(14), 9857-9867. https://doi.org/10.1021/acsomega.1c00554

Ge, J., Zhang, X., Othman, F., Wang, Y., Roshan, H., & Le-Hussain, F. (2020). Effect of fines migration and mineral reactions on CO2-water drainage relative permeability. *International Journal of Greenhouse Gas Control*, *103*, 103184. https://doi.org/https://doi.org/10.1016/j.ijggc.2020.103184

Gordeev, Y. I., Kudryashov, N. A., & Murzenko, V. V. (1987). Flow regimes with temperature extrema is the motion of a gas through a porous medium. *Fluid Dynamics*, *22*(4), 553-559. https://doi.org/10.1007/BF01051419

Hamza, A., Hussein, I. A., Al-Marri, M. J., Mahmoud, M., Shawabkeh, R., & Aparicio, S. (2021). CO2 enhanced gas recovery and sequestration in depleted gas reservoirs: A review. *Journal of Petroleum Science and Engineering*, *196*, 107685. https://doi.org/https://doi.org/10.1016/j.petrol.2020.107685

Jang, M., Chun, T. S., & An, J. (2022). An Analytical Heat Transfer Model in Oil Reservoir during Long-Term Production. *Energies*, *15*(7).

Kacimov, A., & Obnosov, Y. (2023a). Analytical and HYDRUS solutions for exfiltration through inclined seepage faces. *Advances in Water Resources*, *179*, 104517. https://doi.org/https://doi.org/10.1016/j.advwatres.2023.104517

Kacimov, A., & Obnosov, Y. (2023b). Phreatic seepage around a rectilinear cutoff wall: The Zhukovsky-Vedernikov-Polubarinova-Kochina dispute revisited. *Advances in Water Resources*, *173*, 104367. https://doi.org/https://doi.org/10.1016/j.advwatres.2023.104367

Katzourakis, V. E., & Chrysikopoulos, C. V. (2019). Two-site colloid transport with reversible and irreversible attachment: Analytical solutions. *Advances in Water Resources*, *130*, 29-36. https://doi.org/https://doi.org/10.1016/j.advwatres.2019.05.026

Labus, M., & Labus, K. (2018). Thermal conductivity and diffusivity of fine-grained sedimentary rocks. *Journal of Thermal Analysis and Calorimetry*, *132*(3), 1669-1676. https://doi.org/10.1007/s10973-018-7090-5

LaForce, T., Ennis-King, J., & Paterson, L. (2014). Semi-analytical solutions for nonisothermal fluid injection including heat loss from the reservoir: Part 1. Saturation and temperature. *Advances in Water Resources*, *73*, 227-241. https://doi.org/https://doi.org/10.1016/j.advwatres.2014.08.008

Lake, L. W. (1989). *Enhanced oil recovery*. Prentice Hall Englewood Cliffs, N.J.

Lawal, K. A. (2020). Applicability of heat-exchanger theory to estimate heat losses to surrounding formations in a thermal flood. *Journal of Petroleum Exploration and Production Technology*, *10*(4), 1565-1574. https://doi.org/10.1007/s13202-019-00792-5

Machado, M. V. B., Delshad, M., & Sepehrnoori, K. (2023). Injectivity assessment for CCS field-scale projects with considerations of salt deposition, mineral dissolution, fines migration, hydrate formation, and non-Darcy flow. *Fuel*, *353*, 129148. https://doi.org/https://doi.org/10.1016/j.fuel.2023.129148

Mathias, S. A., Gluyas, J. G., Oldenburg, C. M., & Tsang, C.-F. (2010). Analytical solution for Joule–Thomson cooling during CO2 geo-sequestration in depleted oil and gas reservoirs. *International Journal of Greenhouse Gas Control*, *4*(5), 806-810. https://doi.org/https://doi.org/10.1016/j.ijggc.2010.05.008

Miri, R., van Noort, R., Aagaard, P., & Hellevang, H. (2015). New insights on the physics of salt precipitation during injection of CO2 into saline aquifers. *International Journal of Greenhouse Gas Control*, *43*, 10-21. https://doi.org/https://doi.org/10.1016/j.ijggc.2015.10.004

Moghadasi, J., Müller-Steinhagen, H., Jamialahmadi, M., & Sharif, A. (2004). Model study on the kinetics of oil field formation damage due to salt precipitation from injection. *Journal of Petroleum Science and Engineering*, *43*(3), 201-217. https://doi.org/https://doi.org/10.1016/j.petrol.2004.02.014

Moreno, Z., Anto-Darkwah, E., & Rabinovich, A. (2021). Semi-Analytical Modeling of Rate-Dependent Relative Permeability in Heterogeneous Formations. *Water Resources Research*, *57*(4), e2021WR029710. https://doi.org/https://doi.org/10.1029/2021WR029710

Moreno, Z., & Rabinovich, A. (2021). Evaluating numerical simulation errors of CO2-brine flow with capillary heterogeneity using a 1D semi-analytical solution. *International Journal of Greenhouse Gas Control*, *110*, 103416. https://doi.org/https://doi.org/10.1016/j.ijggc.2021.103416

Moreno, Z., & Rabinovich, A. (2021). Impact of Sub-core-scale Heterogeneity on Meter-Scale Flow and Brine Displacement in Drainage by CO2. *Water Resources Research*, *57*(1), e2020WR028332. https://doi.org/https://doi.org/10.1029/2020WR028332

Muradov, K., & Davies, D. (2012). Linear non-adiabatic flow of an incompressible fluid in a porous layer – Review, adaptation and analysis of the available temperature models and solutions. *Journal of Petroleum Science and Engineering*, *86-87*, 1-14. https://doi.org/https://doi.org/10.1016/j.petrol.2012.03.011

Muradov, K. M., & Davies, D. R. (2009). *Temperature Modeling and Analysis of Wells with Advanced Completion* EUROPEC/EAGE Conference and Exhibition, https://doi.org/10.2118/121054-MS

Nguyen, C., Loi, G., Russell, T., Mohd Shafian, S. R., Zulkifli, N. N., Chee, S. C., Razali, N., Zeinijahromi, A., & Bedrikovetsky, P. (2022). Well inflow performance under fines migration during water-cut increase. *Fuel*, *327*, 124887. https://doi.org/https://doi.org/10.1016/j.fuel.2022.124887

Nguyen, M. C., Dejam, M., Fazelalavi, M., Zhang, Y., Gay, G. W., Bowen, D. W., Spangler, L. H., Zaluski, W., & Stauffer, P. H. (2021). Skin factor and potential formation damage from chemical and mechanical processes in a naturally fractured carbonate aquifer with implications to CO2 sequestration. *International Journal of Greenhouse Gas Control*, *108*, 103326. https://doi.org/https://doi.org/10.1016/j.ijggc.2021.103326

Norouzi, A. M., Niasar, V., Gluyas, J. G., & Babaei, M. (2022). Analytical Solution for Predicting Salt Precipitation During CO2 Injection Into Saline Aquifers in Presence of Capillary Pressure. *Water*

Resources Research, *58*(6), e2022WR032612.

https://doi.org/https://doi.org/10.1029/2022WR032612

Oldenburg, C. M. (2007). Joule-Thomson cooling due to CO2 injection into natural gas reservoirs.

Energy Conversion and Management, *48*(6), 1808-1815.

https://doi.org/https://doi.org/10.1016/j.enconman.2007.01.010

Othman, F., Naufaliansyah, M. A., & Hussain, F. (2019). Effect of water salinity on permeability

alteration during CO_2 sequestration. *Advances in Water Resources*, *127*, 237-251.

https://doi.org/https://doi.org/10.1016/j.advwatres.2019.03.018

Parvan, A., Jafari, S., Rahnama, M., Norouzi-Apourvari, S., & Raoof, A. (2021). Insight into particle

detachment in clogging of porous media; a pore scale study using lattice Boltzmann method.

Advances in Water Resources, *151*, 103888.

https://doi.org/https://doi.org/10.1016/j.advwatres.2021.103888

Payne, L. E., & Straughan, B. (1998). Structural stability for the Darcy equations of flow in porous

media. *Proceedings of the Royal Society of London. Series A: Mathematical, Physical and

Engineering Sciences*, *454*(1974), 1691-1698. https://doi.org/10.1098/rspa.1998.0227

Pires, A. P., Bedrikovetsky, P. G., & Shapiro, A. A. (2006). A splitting technique for analytical

modelling of two-phase multicomponent flow in porous media. *Journal of Petroleum Science

and Engineering*, *51*(1), 54-67. https://doi.org/https://doi.org/10.1016/j.petrol.2005.11.009

Polîanin, A. D., & Dil′man, V. V. (1994). *Methods of modeling equations and analogies in chemical

engineering*. CRC Press Boca Raton, Fl.

Polyanin, A., Kutepov, A. M., Vyaz'min, A., & Kazenin, D. A. (2002). *Hydrodynamics, mass and heat

transfer in chemical engineering*.

Polyanin, A., & Nazaikinskii, V. (2016). *Handbook of Linear Partial Differential Equations for

Engineers and Scientists, Second Edition*. https://doi.org/10.1201/b19056

Polyanin, A., & Zaitsev, V. (2003). *Handbook of Nonlinear Partial Differential Equations*.

https://doi.org/10.1201/9780203489659

Rabinovich, A., Itthisawatpan, K., & Durlofsky, L. J. (2015). Upscaling of CO2 injection into brine with capillary heterogeneity effects. *Journal of Petroleum Science and Engineering*, *134*, 60-75. https://doi.org/https://doi.org/10.1016/j.petrol.2015.07.021

Robertson, E. C. (1988). *Thermal properties of rocks* [Report](88-441). (Open-File Report, Issue. U. S. G. Survey. https://pubs.usgs.gov/publication/ofr88441

Schoen, J. (2015). *Physical Properties of Rocks - Fundamentals and Principles of Petrophysics*.

Shapiro, A. A. (2015). Two-Phase Immiscible Flows in Porous Media: The Mesocopic Maxwell–Stefan Approach. *Transport in Porous Media*, *107*(2), 335-363. https://doi.org/10.1007/s11242-014-0442-0

Shapiro, A. A. (2016). Mechanics of the Separating Surface for a Two-Phase Co-current Flow in a Porous Medium. *Transport in Porous Media*, *112*(2), 489-517. https://doi.org/10.1007/s11242-016-0662-6

Shapiro, A. A. (2018). A Three-Dimensional Model of Two-Phase Flows in a Porous Medium Accounting for Motion of the Liquid–Liquid Interface. *Transport in Porous Media*, *122*(3), 713-744. https://doi.org/10.1007/s11242-018-1023-4

Turner, L. G., Dawson, G. K. W., Golding, S. D., & Pearce, J. K. (2022). CO2 and NOx reactions with CO2 storage reservoir core: NOx dissolution products and mineral reactions. *International Journal of Greenhouse Gas Control*, *120*, 103750. https://doi.org/https://doi.org/10.1016/j.ijggc.2022.103750

Van der Velde, R., Mieog, J., Breunese, J., & Remmelts, G. (2008). *Potential for CO2 storage in depleted gas fields on the Dutch Continental Shelf. Phase 1. Technical assessment*.

Vilarrasa, V., & Rutqvist, J. (2017). Thermal effects on geologic carbon storage. *Earth-Science Reviews*, *165*, 245-256. https://doi.org/https://doi.org/10.1016/j.earscirev.2016.12.011

Voronov, V. P., Gorodetskii, E. E., Podnek, V. E., & Grigoriev, B. A. (2016). Properties of equilibrium carbon dioxide hydrate in porous medium. *Chemical Physics*, *476*, 61-68. https://doi.org/https://doi.org/10.1016/j.chemphys.2016.05.031

Xu, A., Mu, L., Fan, Z., Wu, X., Zhao, L., Bo, B., & Xu, T. (2013). Mechanism of heavy oil recovery by cyclic superheated steam stimulation. *Journal of Petroleum Science and Engineering*, *111*, 197-207. https://doi.org/https://doi.org/10.1016/j.petrol.2013.09.007

Yortsos, Y. C., & Gavalas, G. R. (1982). Heat transfer ahead of moving condensation fronts in thermal oil recovery processes. *International Journal of Heat and Mass Transfer*, *25*(3), 305-316. https://doi.org/https://doi.org/10.1016/0017-9310(82)90183-1

Yu, M., Hussain, F., Arns, J. Y., Bedrikovetsky, P., Genolet, L., Behr, A., Kowollik, P., & Arns, C. H. (2018). Imaging analysis of fines migration during water flow with salinity alteration. *Advances in Water Resources*, *121*, 150-161. https://doi.org/https://doi.org/10.1016/j.advwatres.2018.08.006

Yuan, B., & Moghanloo, R. G. (2018). Nanofluid Precoating: An Effective Method To Reduce Fines Migration in Radial Systems Saturated With Two Mobile Immiscible Fluids. *SPE Journal*, *23*(03), 998-1018. https://doi.org/10.2118/189464-PA

Yuan, B., & Moghanloo, R. G. (2019). Analytical modeling nanoparticles-fines reactive transport in porous media saturated with mobile immiscible fluids. *AIChE Journal*, *65*(10), e16702. https://doi.org/https://doi.org/10.1002/aic.16702

Zazovskii, A. F. (1983). Nonisothermal displacement of oil by water from thermally noninsulated strata. *Fluid Dynamics*, *18*(5), 734-741. https://doi.org/10.1007/BF01090996

Ziabakhsh-Ganji, Z., & Kooi, H. (2014). Sensitivity of Joule–Thomson cooling to impure CO2 injection in depleted gas reservoirs. *Applied Energy*, *113*, 434-451. https://doi.org/https://doi.org/10.1016/j.apenergy.2013.07.059

Zolotukhin, A. B. (1979). *Analytical Definition Of The Overall Heat Transfer Coefficient* SPE California Regional Meeting, https://doi.org/10.2118/7964-MS

Appendix A. Derivation of the exact solution

Eq. (13) with IC Eq. (14) and BC Eq. (15) present an initial-boundary value problem for a first-order partial differential equation (PDE) which is solved by the method of characteristics (Polyanin & Zaitsev, 2003).

Considering the piston-like displacement of water by CO_2, two temperature domains are delineated by a shock front. First, we consider the domain ahead of the heat front, where IC propagates along the characteristic lines. Here the free variable is the dimensionless time, t_D.

Assuming that, $T_D = T^*(r_D(t_D), t_D)$, the total derivative of T^* with respect to t_D is obtained as:

$$\frac{dT^*}{dt_D} = \frac{\partial T_D}{\partial r_D}\frac{dr_D}{dt_D} + \frac{\partial T_D}{\partial t_D} = -A^*\frac{1}{r_D{}^2} - (T^* - 1) \tag{A1}$$

Therefore, the domain ahead of heat front is defined by a system of first order ODE as:

$$\frac{dr_D}{dt_D} = \frac{V^*}{r_D} \;\; ; \;\; \frac{dT^*}{dr_D} = \frac{r_D}{V^*}\left(-A^*\frac{1}{r_D{}^2} - (T^* - 1)\right) \tag{A2}$$

The system of equations Eq. (A2) is solved with the following IC:

$$t_D = 0: T^* = T_D(r_{D0}, 0) = 1 \tag{A3}$$

By integrating the first part of the system of equations Eq. (A2), we obtain the trajectory of characteristics as:

$$t_D = \frac{r_D{}^2 - 1}{2V^*} - \frac{r_{D0}}{V^*} \tag{A4}$$

Further, we solve the second part of the system of equations Eq (A2) to obtain a general solution for temperature in the domain $t_D < \frac{r_D{}^2 - 1}{2V^*}$ as:

$$T^* = 1 - \frac{A^*}{2V^*}Ei\left(\frac{r_D{}^2}{2V^*}\right)e^{-\frac{r_D{}^2}{2V^*}} + c_1 e^{-\frac{r_D{}^2}{2V^*}} \tag{A5}$$

Here, the $Ei(x)$ function is defined as:

$$Ei(x) = \int_{-\infty}^{x}\frac{e^t}{t}dt, a < b, \int_{a}^{b}\frac{e^t}{t}dt = \int_{-\infty}^{b}\frac{e^t}{t}dt - \int_{-\infty}^{a}\frac{e^t}{t}dt = Ei(b) - Ei(a) \tag{A6}$$

By using the IC Eq. (A3), the constant of integration c_1 in Eq. (A5) is obtained as:

$$c_1 = \frac{A^*}{2V^*}Ei\left(\frac{r_D{}^2}{2V^*} - t_D\right) \tag{A7}$$

By substituting Eq. (A7) into the general solution Eq. (A5), the temperature profile in the domain ahead of the heat front is obtained as:

$$T_D(r_D, t_D) = 1 - \frac{A^*}{2V^*}Ei\left(\frac{r_D{}^2}{2V^*}\right)e^{-\frac{r_D{}^2}{2V^*}} + \left[\frac{A^*}{2V^*}Ei\left(\frac{r_D{}^2}{2V^*}\right)\right]e^{-\frac{r_D{}^2}{2V^*}} \tag{A8}$$

Next, we consider the domain behind of the heat front, where BC propagates along the characteristic lines. Here the free variable is the dimensionless radius, r_D. Assuming that, $T_D = \bar{T}(r_D, t_D(r_D))$, the total derivative of $\bar{T}$ with respect to r_D is obtained as:

$$\frac{d\bar{T}}{dr_D} = \frac{\partial T_D}{\partial r_D} + \frac{\partial T_D}{\partial t_D}\frac{dt_D}{dr_D} = \frac{1}{V^*}\left(-A^*\frac{1}{r_D{}^2} - (\bar{T} - 1)\right) \tag{A9}$$

Therefore, the following system of first order ODE is obtained for the domain behind of the heat front.

$$\frac{dt_D}{dr_D} = \frac{r_D}{V^*} \quad ; \quad \frac{d\bar{T}}{dr_D} = r_D\left[\frac{1}{V^*}\left(-A^*\frac{1}{r_D{}^2} - (\bar{T} - 1)\right)\right] \tag{A10}$$

In this domain, the system of equations Eq. (A10) is solved with the following BC:

$$r_D = 1: \bar{T} = T_D(0, t_{D0}) = \frac{T_J}{T_I} \tag{A11}$$

By integrating the first part of the system of equations Eq. (A10), the trajectory of characteristics is:

$$t_D = \frac{r_D{}^2 - 1}{2V^*} + t_{D0} \tag{A12}$$

Additionally, we solve the second part of the system of equations Eq (A10) to obtain a general solution for temperature in the domain $t_D > \frac{r_D{}^2 - 1}{2V^*}$ as:

$$\bar{T} = 1 - \frac{A^*}{2V^*}Ei\left(\frac{r_D{}^2}{2V^*}\right)e^{-\frac{r_D{}^2}{2V^*}} + c_2 e^{-\frac{r_D{}^2}{2V^*}} \tag{A13}$$

By using the BC Eq. (A11), the constant of integration c_2 in Eq. (A13) is obtained as:

$$c_2 = \left(\frac{T_J - T_I}{T_I}\right)e^{\frac{1}{2V^*}} + \frac{A^*}{2V^*}Ei\left(\frac{1}{2V^*}\right) \tag{A14}$$

By substituting Eq. (A14) into the general solution Eq. (A13), the temperature profile in the domain behind the heat front is obtained as:

$$T_D(r_D, t_D) = 1 - \frac{A^*}{2V^*}Ei\left(\frac{r_D{}^2}{2V^*}\right)e^{-\frac{r_D{}^2}{2V^*}} + \left[\left(\frac{T_J - T_I}{T_I}\right)e^{\frac{1}{2V^*}} + \frac{A^*}{2V^*}Ei\left(\frac{1}{2V^*}\right)\right]e^{-\frac{r_D{}^2}{2V^*}} \tag{A15}$$

Finally, the shock emanates from the point (1,0) in the r_D - t_D plane; which allows for the overall dimensionless solution for the problem defined by Eq. (13) with IC Eq. (14) and BC Eq. (15) to be obtained as:

$$T_D(r_D, t_D) = \begin{cases} 1 - \frac{A^*}{2V^*} Ei\left(\frac{r_D{}^2}{2V^*}\right) e^{-\frac{r_D{}^2}{2V^*}} + \left[\left(\frac{T_J - T_I}{T_I}\right) e^{\frac{1}{2V^*}} + \frac{A^*}{2V^*} Ei\left(\frac{1}{2V^*}\right)\right] e^{-\frac{r_D{}^2}{2V^*}}; & t_D > \frac{r_D{}^2 - 1}{2V^*} \\ 1 - \frac{A^*}{2V^*} Ei\left(\frac{r_D{}^2}{2V^*}\right) e^{-\frac{r_D{}^2}{2V^*}} + \left[\frac{A^*}{2V^*} Ei\left(\frac{r_D{}^2}{2V^*} - t_D\right)\right] e^{-\frac{r_D{}^2}{2V^*}}; & t_D < \frac{r_D{}^2 - 1}{2V^*} \end{cases} \tag{A16}$$

The substitution of the dimensionless parameters in Eqs. (10-12) into Eq. (A16) yields the dimensional form of the solution as:

$$T(r,t) = \begin{cases} T_I + (T_J - T_I)e^{-\frac{B}{V}\pi(r^2 - r_w{}^2)} + \frac{\alpha_{JT}\mu_f q_J}{4\pi k_{rf}^e kH}\left[Ei\left(\frac{B}{V}\pi r_w{}^2\right) - Ei\left(\frac{B}{V}\pi r^2\right)\right]e^{-\frac{B}{V}\pi r^2}; & \pi r^2 < \pi r_w{}^2 + V q_J t \\ T_I + \frac{\alpha_{JT}\mu_f q_J}{4\pi k_{rf}^e kH}\left\{Ei\left(\frac{B}{V}(\pi r^2)\right) - Ei\left(\frac{B}{V}\pi r^2\right)\right\}e^{-\frac{B}{V}\pi r^2}; & \pi r^2 > \pi r_w{}^2 + V q_J t \end{cases}$$

$$\tag{A17}$$

Appendix B. Exact solution for heat exchange in the adjacent layers of semi-infinite thickness

The assumptions of the quasi 2D heat conductivity problem in adjacent layers comprise: No horizontal heat transfer, i.e. $\gamma_x = 0$; constant vertical heat conductivity $\gamma_z = \gamma = const$; thickness of the shale is much smaller than the thickness of the reservoir and the adjacent layers. The equation that governs heat transfer along the vertical direction in the adjacent formations above and below the reservoir is expressed in the form:

$$(\phi_a \rho_w c_w + (1 - \phi_a)\rho_{ra} c_{ra})\frac{\partial T(r,z,t)}{\partial t} = (\phi_a \gamma_w + (1 - \phi_a)\gamma_{ra})\frac{\partial^2 T(r,z,t)}{\partial z^2}, \ 0 < z < \infty \tag{B1}$$

Here, ϕ_a is adjacent layers porosity, ρ_{ra} [ML^{-3}] is adjacent layers rock density, c_{ra} [L^{2}T^{-2}K^{-1}] is the specific heat capacity of adjacent layers rock, γ_w [MLT^{-3}K^{-1}] is thermal conductivity of water, γ_{ra} [MLT^{-3}K^{-1}] is thermal conductivity of adjacent layers and z [L] is distance in the vertical direction.

Further, the thermal diffusivity during the heat transfer is defined as:

$$a_a = \frac{\phi_a \gamma_w + (1 - \phi_a)\gamma_{ra}}{\phi_a \rho_w c_w + (1 - \phi_a)\rho_{ra} c_{ra}} = \frac{\gamma^a}{c^a} \tag{B2}$$

Substituting Eq. (B2) into Eq. (B1), the heat transfer equation is reformulated to the form:

$$\frac{\partial T(r,z,t)}{\partial t} = a_a \frac{\partial^2 T(r,z,t)}{\partial z^2}, \ 0 < z < \infty \tag{B3}$$

The initial condition (IC) corresponding to the equality of temperature in all formations is given as:

$$T(r, z, t = 0) = T_I \tag{B4}$$

Additionally, the boundary conditions (BCs) for the semi-infinite vertical domain is defined as:

$$T(r, z \rightarrow \infty, t) = T_I \tag{B5}$$

$$\frac{\partial T}{\partial z}(r, z = 0, t) = -\frac{\gamma^s}{\gamma^a}\frac{1}{l}[T(r = const., t) - T(r, z = 0, t)] \tag{B6}$$

Here, γ^s denotes the overall shale heat conductivity and it is given as:

$$\gamma^s = \phi_s \gamma_w + (1 - \phi_s)\gamma_{rs} \tag{B7}$$

Also, $T(r = const., t)$ denotes the temperature in the reservoir post injection (taken at constant radial distances from injection well). We further define the overall reservoir volumetric heat capacity as:

$$c^{res} = \phi(1 - S_{wi})\rho_f c_f + \phi S_{wi}\rho_w c_w + (1 - \phi)\rho_s c_s \tag{B8}$$

In this work, we introduce a new dimensionless parameter, $\omega = f(\gamma, c, H, l)$, which establishes a ratio of for the following properties; heat conductivity, heat capacity and thickness of the reservoir and the shale

$$\omega = \sqrt{\frac{c^{res}\gamma^s H}{c^a \gamma^a l}} \tag{B9}$$

In addition, we consider the following dimensionless variables to nondimensionalize Eqs. (B3 - B6):

$$t_D = \frac{\gamma^s t}{Hlc^{res}} \; ; \; z_D = \frac{z}{\sqrt{\frac{Hlc^{res}\gamma^a}{\gamma^s}\frac{}{c^a}}} \; ; \; \theta = \frac{T}{T_I} \tag{B10}$$

Using Eq. (B10), the second order PDE Eq (B3) together with the IC Eq. (B4) and BCs Eqs. (B5 - B6) are respectively expressed in dimensionless form as:

$$\frac{\partial \theta}{\partial t_D} = \frac{\partial^2 \theta}{\partial z_D^2} \; , \; 0 < z_D < \infty \tag{B11}$$

$$\theta(z_D, t_D = 0) = 1 \tag{B12}$$

$$\theta(z_D \rightarrow \infty, t_D) = 1 \tag{B13}$$

$$\frac{\partial \theta}{\partial z_D}(z_D = 0) - \omega\theta(z_D = 0) = -\omega T_D(r_D = const.) \tag{B14}$$

The details of the solution to the problem defined by Eqs. (B11 - B14) is expounded in the work of Polyanin and Nazaikinskii (2016). Based on the approach discussed by Polyanin and Nazaikinskii (2016), the general solution to the second order problems of this kind is obtained as:

$$T(z,t) = \int_0^\infty f(x)G(z,x,t)dx - a_a \int_0^t g(\tau)G(z,0,t-\tau)d\tau \qquad \text{(B15)}$$

Here, $f(x)$ and $g(\tau)$ are arbitrary functions of x and τ, respectively and the function $G(z,x,t)$ is defined as:

$$G(z,x,t) = \frac{1}{2\sqrt{\pi a_a t}}\left\{e^{-\frac{(z-x)^2}{4a_a t}} + e^{-\frac{(z+x)^2}{4a_a t}} - 2k\left[\sqrt{\pi a_a t}\,e^{a_a k^2 t + k(z+x)}erfc\left(\frac{z+x}{2\sqrt{a_a t}} + k\sqrt{a_a t}\right)\right]\right\} \qquad \text{(B16)}$$

$$G(z,0,t-\tau) = \frac{1}{\sqrt{\pi a_a(t-\tau)}}\left\{e^{-\frac{z^2}{4a_a(t-\tau)}} - k\left[\sqrt{\pi a_a(t-\tau)}\,e^{a_a k^2(t-\tau)+kz}erfc\left(\frac{z}{2\sqrt{a_a(t-\tau)}} + k\sqrt{a_a(t-\tau)}\right)\right]\right\} \qquad \text{(B17)}$$

From the general solution given by Eq. (B15), together with Eqs. (B16 - B17), the solution to the heat transfer problem Eqs. (B11 - B14) is obtained as:

$$\theta(z_D,t_D) = erf\left(\frac{z_D}{2\sqrt{t_D}}\right) + e^{\omega^2 t_D + \omega z_D}erfc\left(\frac{z_D}{2\sqrt{t_D}} + \omega\sqrt{t_D}\right) +$$

$$\omega \int_0^{t_D} \frac{T_D(r_D=const.,\tau)}{\sqrt{\pi(t_D-\tau)}}\left\{e^{-\frac{z_D^2}{4(t_D-\tau)}} - \omega\left[\sqrt{\pi(t_D-\tau)}\,e^{\omega^2(t_D-\tau)+\omega z_D}erfc\left(\frac{z_D}{2\sqrt{(t_D-\tau)}} + \omega\sqrt{(t_D-\tau)}\right)\right]\right\}d\tau \qquad \text{(B18)}$$

The value for temperature $\theta(z_D,t_D)$ on the interface between an adjacent layers and shale is obtained by setting $z_D = 0$ in Eq. (B18) to obtain:

$$\theta(z_D = 0, t_D) = e^{\omega^2 t_D}erfc(\omega\sqrt{t_D}) +$$

$$\omega \int_0^{t_D} \frac{T_D(r_D=const.,\tau)}{\sqrt{\pi(t_D-\tau)}}\left\{1 - \omega\left[\sqrt{\pi(t_D-\tau)}\,e^{\omega^2(t_D-\tau)}erfc(\omega\sqrt{(t_D-\tau)})\right]\right\}d\tau \qquad \text{(B19)}$$

where,

$$T_D(r_D = const.,\tau) = \begin{cases} 1 + \left[\left(\frac{T_J-T_I}{T_I}\right)e^{\frac{1}{2V^*}} + \frac{A^*}{2V^*}\left(Ei\left(\frac{1}{2V^*}\right) - Ei\left(\frac{r_D^2}{2V^*}\right)\right)\right]e^{-\frac{r_D^2}{2V^*}} & t_D > \frac{r_D^2-1}{2V^*} \\[3mm] 1 - \frac{A^*}{2V^*}e^{-\frac{r_D^2}{2V^*}}\left[Ei\left(\frac{r_D^2}{2V^*}\right) - Ei\left(\frac{r_D^2}{2V^*} - \tau\right)\right] & \frac{r_D^2-1}{2V^*} < t_D \end{cases} \qquad \text{(B20)}$$